PAPER

Perfect cubic metallo-borospherenes TM$_8$B$_6$ (TM = Ni, Pd, Pt) as superatoms following the 18-electron rule†

Mei-Zhen Ao,[ab] Yuan-Yuan Ma,[c] Yue-Wen Mu [ID] *[a] and Si-Dian Li [ID] *[a]

Transition-metal (TM)-doped metallo-borospherenes exhibit unique structures and bonding in chemistry which have received considerable attention in recent years. Based on extensive global minimum searches and first-principles theory calculations, we predict herein the first and smallest perfect cubic metallo-borospherenes O_h TM$_8$B$_6$ (TM = Ni (**1**), Pd (**2**), Pt (**3**)) and O_h Ni$_8$B$_6^-$ (**1**$^-$) which contain eight equivalent TM atoms at the vertexes of a cube and six quasi-planar tetra-coordinate face-capping boron atoms on the surface. Detailed canonical molecular orbital and adaptive natural density partitioning bonding analyses indicate that O_h TM$_8$B$_6$ (**1/2/3**) as superatoms possess nine completely delocalized 14c−2e bonds following the 18-electron principle (1S^{2}1P^{6}1D^{10}), rendering spherical aromaticity and extra stability to the complex systems. Furthermore, Ni$_8$B$_6$ (**1**) can be used as building blocks to form the three-dimensional metallic binary crystal NiB (**4**) ($Pm\bar{3}m$) in a bottom-up approach which possesses a typical CsCl-type structure with an octa-coordinate B atom located exactly at the center of the cubic unit cell. The IR, Raman, UV-vis and photoelectron spectra of the concerned clusters are computationally simulated to facilitate their experimental characterization.

Introduction

As a typical electron-deficient element, boron exhibits unique structures and bonding in both polyhedral molecules and bulk allotropes.[1] Researchers have spared no efforts to explore the possibility of all-boron fullerenes since the discovery of buckminsterfullerene (C$_{60}$) in 1985.[2] The first theoretically proposed perfect cage-like I_h B$_{80}$ fullerene (which is, in fact, not a true minimum of the system) iso-valent with C$_{60}$ was later proved to favour core–shell structures in thermodynamics at the density functional theory (DFT) level.[3,4] The first all-boron fullerenes or borospherenes D_{2d} B$_{40}^{-/0}$ were discovered in 2014 by joint experimental and theoretical investigations, followed by the experimental observations of the axially chiral borospherenes C_3 B$_{39}^-$ and C_2 B$_{39}^-$, seashell-like C_2 B$_{28}^{-/0}$, and bilayer D_{2h} B$_{48}^{-/0}$.[5–8] Cage-like C_1 B$_{41}^+$, C_2 B$_{42}^{2+}$, C_s B$_{38}^{2-}$, C_s B$_{37}^{3-}$ and T_h B$_{36}^{4-}$ were also later predicted at the first-principles theory level, presenting a B$_n^q$ (n = 36–42, q = n − 40) borospherene family in boron nanoclusters.[9–12] Transition-metal-doping has proven to induce dramatic structural and bonding pattern changes in boron

^{a}*Nanocluster Laboratory, Institute of Molecular Science, Shanxi University, Taiyuan 030006, P. R. China*

^{b}*Fenyang College of Shanxi Medical University, Fenyang 032200, China. E-mail: ywmu@sxu.edu.cn; lisidian@sxu.edu.cn*

^{c}*Shanxi Institute of Energy, Taiyuan 030006, China*

† Electronic supplementary information (ESI) available. See DOI: https://doi.org/10.1039/d3na00551h

clusters.[13,14] Exohedral metallo-borospherenes C_s M ∈ B$_{40}$ (M = Be, Mg) with a quasi-planar hepta-coordinate metal center in an η^7-B$_7$ heptagon on the cage surface were the first metallo-borospherenes predicted in theory.[15] The first experimentally observed spherical trihedral metallo-borospherene La$_3$B$_{18}^-$ with three equivalent deca-coordinate La atoms as integral parts of the cage surface was later extended to the smallest core–shell-like metallo-borospherene D_{3h} La$_3$B$_{20}^-$ (La$_3$ & [B$_2$@B$_{18}$]$^-$) which contains a B$_2$ core at the center at the first principles theory level.[16,17] The smallest metallo-borospherene D_{3h} Ta$_3$B$_{12}^-$ with three equivalent octa-coordinate Ta centers in three η^8-B$_8$ rings was also reported in theory.[18] The recently reported Archimedean beryllo-borospherene Be$_4$B$_{12}^+$ was a truncated tetrahedron with four B$_6$ rings capped with four beryllium atoms.[19] Exohedral metallo-borospherene T_d Ta$_4$B$_{18}$ and endohedral metallo-borospherene D_{2d} U@B$_{40}$ were predicted at the DFT level to be superatoms following the 18-electron rule and 32-electron rule, respectively.[20,21] Bottom-up approaches were recently proposed at the DFT level from medium-sized bilayer boron nanoclusters to bilayer borophene nanomaterials[22] and from heptacoordinate transition-metal-decorated metallo-borospherenes to quasi-multiple-helix metallo-boronanotubes.[23]

Cubic Zn$_8^I$-bearing compounds [Zn$_8^I$(HL)$_4$(L)$_8$]$^{12-}$ (L = tetrazole dianion) have been experimentally observed, where the aromatic cubic [Zn$_8^I$] motif can be used as building blocks to form self-assembled materials.[24] Transition metal (TM) clusters based on a TM$_8$ cube with twelve organic ligands on twelve edges have been extensively studied.[25–27] A three-dimensional

aromatic C_i Li_8B_6 was proposed which contains eight Li-atoms on the eight triangular faces of a distorted B_6 octahedron.[28] Recently, a perfect cubic O_h CBe_8H_{12} with an octa-coordinate carbon at the center was predicted at the DFT level as a superatom following a two-fold superatomic electron configuration ($1S^21P^62S^22P^62D^{10}2F^6$).[29] However, transition-metal–non-metal binary clusters with face-capping non-metal atoms on the six tetragonal faces of a perfect TM_8 cube still remain unknown to date in both theory and experiments. It is interesting and important to ask at the current stage whether perfect cubic TM_8B_6 clusters with six face-capping B atoms on the tetragonal faces of a TM_8 cube can be formed and whether such cubic complexes can be used as building blocks to form boron-based low-dimensional nanomaterials in bottom-up approaches.

Based on extensive GM searches and first-principles theory calculations, we predicted in this work a series of perfect cubic metallo-borospherenes O_h TM_8B_6 (TM = Ni (1), Pd (2), Pt (3)) and monoanion O_h $Ni_8B_6^-$ (1^-) which contain eight TM atoms at the vertexes of a cube and six quasi-planar tetra-coordinate face-capping boron atoms on the surface. These high-symmetry metallo-borospherenes TM_8B_6 (1/2/3) satisfy the 18-electron principle ($1S^21P^61D^{10}$) in electron configurations and are spherically aromatic in nature. In addition, the structural motif of aromatic cubic Ni_8B_6 (1) can be extended to construct the metallic three-dimensional (3D) crystal NiB (4) ($Pm\bar{3}m$) in a bottom-up approach which possesses a characteristic CsCl-type structure with an octa-coordinate B atom located exactly at the center of the cubic unit cell.

Computational details

Extensive GM searches are performed on TM_8B_6 (TM = Ni, Pd, Pt) using the TGmin2 program,[30] in conjunction with manual structural constructions. More than 3000 trial structures were explored for each species on their respective potential energy surfaces in both singlet and triplet states at the PBE/TZVP level. The resulting low-lying isomers for TM_8B_6 (TM = Ni, Pd, Pt) were then fully optimized using both PBE0 (ref. 31) and TPSSh[32] methods with the 6-311+G(d)[33] basis set for B and Ni and Stuttgart relativistic small-core pseudopotential for Pd and Pt.[34] Vibrational frequencies of low-lying isomers were checked at the same level to ensure that the reported isomers were true minima on the potential surfaces. The UV-vis and photoelectron (PE) spectra were simulated using the time-dependent TD-DFT-PBE0 approach.[35] All the DFT calculations in this work were implemented using the Gaussian 09 program.[36] Wiberg bond indices (WBIs) and natural atomic charges were obtained by natural bond orbital (NBO) analyses using the NBO 6.0 program.[37] Born–Oppenheimer molecular dynamics (BOMD) simulations with a time step of 1 fs in 30 000 steps were carried out with the GTH-PBE pseudopotential and the TZVP-MOLOPTSR-GTH basis set employing the CP2K code.[38] Chemical bonding patterns were elucidated by canonical molecular orbital (CMO) and adaptive natural density partitioning (AdNDP) analyses.[39] Nucleus independent chemical shifts (NICSs)[40,41] and iso-chemical shielding surfaces (ICSSs) were

computed to reveal the aromaticity of the concerned systems. Orbital compositions and ICSSs were examined using Multiwfn 3.7 code.[42] The visualization for the isosurfaces of various functions was realized with VMD software.[43]

First-principles calculations on 3D crystal NiB (4) were performed using the Vienna *ab initio* simulation package (VASP),[44,45] within the framework of the projector augmented wave (PAW)[46,47] pseudopotential method and PBE generalized gradient approximation (GGA).[48,49] The energy cutoff of plane waves was set to 450 eV. Atomic structures were fully relaxed using the conjugate gradient method until the maximum force on each atom was less than 0.01 eV $Å^{-1}$ and the energy precision was set to 10^{-5} eV per atom. The Brillouin zone was sampled by $25 \times 25 \times 25$ and $32 \times 32 \times 32$ *k*-point meshes with the Monkhorst–Pack scheme for geometry optimizations and further calculations on electronic properties, respectively. The Coulomb-corrected local spin density approximation (LSDA + U) was utilized for both structural optimizations and static calculation with the Hubbard value of $U = 6$ eV for Ni.[50–53] The phonon spectrum was calculated using the finite displacement method with the Phonopy code combined with VASP at the PBE level.[54]

Results and discussion

Structures and stabilities

The obtained singlet GM structures of O_h Ni_8B_6 (1, $^1A_{1g}$), O_h Pd_8B_6 (2, $^1A_{1g}$) and O_h Pt_8B_6 (3, $^1A_{1g}$) are collectively depicted in Fig. 1, with more alternative low-lying isomers tabulated in Fig. S1–S3.† Metallo-borospherenes 1/2/3 possess perfect cubic structures with eight TM atoms (TM = Ni, Pd, Pt) on the vertexes of a cube and six quasi-planar tetra-coordinate face-capping B atoms on the surface, presenting the first and smallest perfect cubic metallo-borospherenes reported to date. 1/2/3 have the smallest vibrational frequencies of 124.4/90.3/54.6 cm^{-1} and large calculated HOMO–LUMO energy gaps of $\Delta E_{gap} = 2.31/2.50/2.96$ eV at the PBE0/6-311+G(d) level, respectively, well supporting their high chemical stabilities. 1/2/3 possess the optimized TM–B bond lengths of $r_{TM-B} = 1.91/2.07/2.08$ Å and calculated Wiberg bond orders of WBI = 0.53/0.45/0.54,

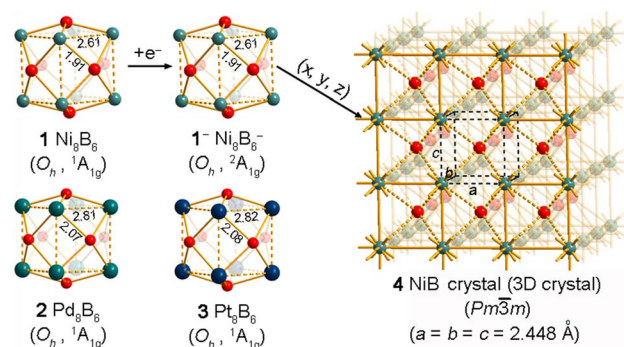**Fig. 1** Optimized structures of O_h Ni_8B_6 (1), O_h $Ni_8B_6^-$ (1^-), O_h Pd_8B_6 (2), and O_h Pt_8B_6 (3) clusters at the PBE0 level and 3D NiB (4) crystal assembled from the structural motif of Ni_8B_6 (1) at the GGA–PBE level, with the necessary bond lengths and lattice parameters indicated in Å.

respectively. These distances are very close to the standard TM–B single bond lengths (1.95, 2.05, and 2.08 Å for TM = Ni, Pd, and Pt, respectively).[55] Interestingly, with the calculated total Wiberg bond orders of WBI = 3.71/3.38/3.52, the face-capping B atoms in **1**/**2**/**3** can be viewed as quasi-planar tetra-coordinate B atoms interconnected by the triply coordinated TM atoms at the corners, while with the TM–TM distances of r_{TM-TM} = 2.61/2.81/2.82 Å and Wiberg bond orders of WBI = 0.13, 0.06, and 0.08 in **1**/**2**/**3**, the weak TM–TM covalent interactions in these complex clusters can be practically neglected. Extensive structural searches indicate that O_h Ni_8B_6 (**1**, $^1A_{1g}$) is the well-defined GM of the system, being at least 0.66 eV more stable than other low-lying isomers. Its slightly distorted C_{2h} triplet counterpart (**1b**) and C_{2v} quintet counterpart (**1l**) due to the Jahn–Teller effect are 0.66 and 1.38 eV less stable than **1** at the PBE0 level, respectively (Fig. S1†). Similarly, both singlet O_h Pd_8B_6 (**2**, $^1A_{1g}$) and O_h Pt_8B_6 (**3**, $^1A_{1g}$) are true GMs of the systems and are at least 0.21 and 1.11 eV more stable than their nearest counterparts at the PBE0 level, respectively (Fig. S2 and S3†). Interestingly, as collectively shown in Fig. S1–S3,† the top fourteen low-lying isomers of TM_8B_6 (TM = Ni/Pd/Pt) within 1.45/1.75/1.61 eV all possess cage-like structures. Attachment of one extra electron to O_h Ni_8B_6 (**1**, $^1A_{1g}$) generates its doublet monoanion O_h $Ni_8B_6^-$ (**1⁻**, $^2A_{1g}$) which maintains the same symmetry as O_h Ni_8B_6 (**1**) with a non-degenerate singly occupied SOMO (a_{1g}) originating from the LUMO (a_{1g}) of the neutral O_h Ni_8B_6 (Fig. 3(a)). As clearly shown in Fig. S4,† O_h $Ni_8B_6^-$ (**1⁻**) is also the well-defined GM of the monoanion which lies 0.40 eV lower than its second lowest-lying counterpart.

Extensive BOMD simulations were performed to check the dynamic stabilities of these cubic metallo-borospherenes. As shown in Fig. S5,† **1**, **2**, and **3** are dynamically stable at 600, 600, and 500 K, respectively, with the small calculated root-mean-square-deviations of RMSD = 0.11, 0.10, and 0.10 Å and maximum bond length deviations of MAXD = 0.29, 0.30, and 0.28 Å. The structural integrities of these metallo-borospherenes are well maintained during the BOMD simulations, with no high energy isomers observed for the 30 ps in the simulating processes.

As demonstrated in Fig. 1, the structural motif of Ni_8B_6 (**1**) can be extended in three (x, y, z) dimensions periodically to form the 3D NiB (**4**) ($Pm\bar{3}m$) in a bottom-up approach which possesses a typical CsCl-type crystal structure with the optimized lattice parameters of $a = b = c = 2.448$ Å at the GGA-PBE level. To evaluate the relative stabilities of 3D Ni_mB_n crystals, we computed their average cohesive energy per atom (E_{coh}) using the formula $E_{coh} = (mE_{Ni} + nE_B - E_{Ni_mB_n})/(m + n)$, where $E_{Ni_mB_n}$, E_B, and E_{Ni} are the total energies of Ni_mB_n, a doublet B atom, and a triplet Ni atom, and m and n are the numbers of Ni and B atoms in the unit cell, respectively. 3D NiB (**4**) has the calculated cohesive energies of E_{coh} = 4.57 eV per atom which is obviously higher than the corresponding value of E_b = 3.41 eV per atom obtained for the O_h Ni_8B_6 (**1**) cluster, though it is slightly lower than the corresponding value of E_{coh} = 4.86 eV per atom calculated for the experimentally reported Ni_4B_4 crystal ($Cmmm$).[56] As a true minimum of 3D Ni–B binary crystals, NiB (**4**) contains an octa-coordinate B atom located exactly at the
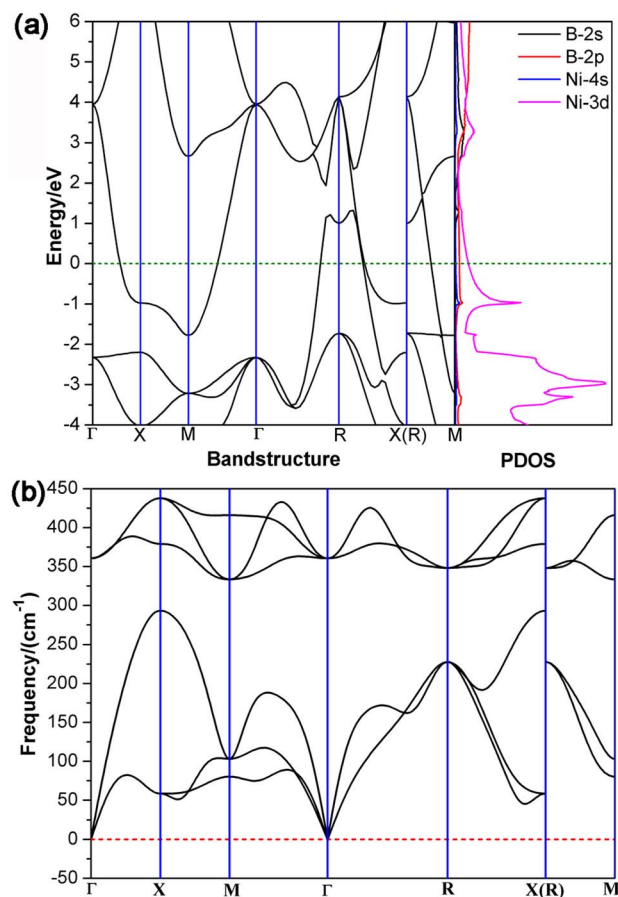

Fig. 2 (a) Calculated band structures and PDOS of 3D NiB (**4**) and (b) calculated phonon dispersion curves of a 4 × 4 × 4 supercell of 3D crystal NiB (**4**) at the GGA-PBE level.

center of the cubic unit cell with the Ni–B coordination bond length of r_{Ni-B} = 2.120 Å. The calculated band structures and projected densities of states (PDOS) of 3D NiB (**4**) depicted in Fig. 2(a) clearly indicate that NiB (**4**) is metallic in nature, with Ni-3d orbitals contributing mainly to the calculated densities of states near the Fermi level. The calculated phonon dispersion curves of NiB (**4**) with a 4 × 4 × 4 supercell in Fig. 2(b) exhibit clearly no imaginary frequencies, demonstrating its high dynamical stability. Detailed Bader charge analyses indicate that the central B atom and vertex Ni atom possess the average atomic charge of $q_B = -0.22|e|$ and $q_{Ni} = +0.22|e|$, respectively, similar overall to the charge distribution in Ni_8B_6 (**1**).

Bonding analyses of metallo-borospherenes

Detailed NBO analyses were performed on these cubic complexes to better comprehend their high stabilities. B atoms in **1**/**2**/**3** all possess negative calculated net atomic charges of $q_B = -0.809--0.313|e|$ and electronic configurations of $[He]2s^{1.30-1.41}2p^{1.88-2.32}$, while the TM atoms have the corresponding positive net atomic charges of $q_{TM} = +0.232-+0.607|e|$ and electronic configurations of $Ni[Ar]3d^{9.06}4s^{0.33}$, $Pd[Kr]4d^{9.43}5s^{0.35}$, and $Pt[Xe]5d^{9.29}6s^{0.49}$, respectively. These NBO results indicate that TM atoms on the vertexes donate

approximately one and a half electrons from their 4s/5s/6s atomic orbitals to the face-capping B atoms, while, in return, they accept roughly one electron in their partially filled 3d/4d/5d orbitals from the surrounding B atoms *via* effective B(2p) → Ni(3d) backdonations, suggesting the formation of effective electron delocalization in these complexes. To help unveil the bonding nature of these cubic metallo-borospheres, we further analysed the frontier molecular orbitals (MOs) and densities of states (DOS) of O_h Ni_8B_6 (**1**). As clearly shown in Fig. 3(a), the fully filled non-degenerate HOMO−14 (a_{1g}) of Ni_8B_6 (**1**) ($1S^2$) exhibits no nodal plane on the cube surface, the triply degenerate HOMO−9 (t_{1u}) (P_x^2, P_y^2, and P_z^2) has one nodal plane, and the doubly degenerate HOMO−1 (e_g) ($D_{x^2−y^2}$ and $D_{z^2}^2$) and triply degenerate HOMO (t_{2g}) (D_{xz}^2, D_{yz}^2, and D_{xy}^2) possess two nodal planes. Such an orbital occupation of the cubic complex well corresponds to the electronic configuration of $1S^21P^61D^{10}$ of a superatom in a cubic coordination field. It is noticed that Ni-3d orbitals contribute 67.5–83.5% to these totally delocalized molecular orbitals. As shown in Fig. 3(a), Ni-3d orbitals also make the major contribution to the overall density of states of the complex.

Detailed AdNDP bonding analyses of O_h Ni_8B_6 (**1**) shown in Fig. 3(b) unveil clearly the one-center–two-electron (1c–2e) lone pairs, two-center–two-electron (2c–2e) localized bonds, and fourteen-center–two-electron (14c–2e) delocalized bonds in the complex. Ni_8B_6 (**1**) possesses 49 pairs of valence electrons in 49 bonds in total. As shown in the first row of Fig. 3(b), each Ni atom at the vertex in Ni_8B_6 (**1**) carries two 1c–2e lone pairs in vertical and horizontal directions ($3d_{z^2}$ and $3d_{x^2−y^2}$) with the occupation numbers of ON ≈ 1.84$|e|$. There exist four equivalent localized 2c–2e Ni–B σ bonds around each quasi-planar tetra-coordinate face-capping B atom with ON = 1.95$|e|$. The remaining 18 electrons are totally delocalized in nine delocalized 14c–2e bonds in O_h Ni_8B_6 (**1**) with ON = 2.00$|e|$, including 1 14c–2e S-type bond (1S), 3 14c–2e P-type bonds ($1P_x$, $1P_y$, and $1P_z$), and 5 14c–2e D-type bonds ($1D_{xz}$, $1D_{yz}$, $1D_{xy}$, $1D_{x^2−y^2}$, and $1D_{z^2}$). Similar to the nine totally delocalized MOs depicted in Fig. 3(a), such an AdNDP bonding pattern with nine totally delocalized 14c–2e bonds further indicates that Ni_8B_6 (**1**) as a superatom follows the 18-electron principle ($1S^21P^61D^{10}$). As clearly shown in Fig. S6,† both Pd_8B_6 (**2**) and Pt_8B_6 (**3**) possess similar superatomic molecular orbital occupations and AdNDP bonding patterns to Ni_8B_6 (**1**).

Such bonding patterns render spherical aromaticity to cubic metallo-borospherenes **1**/**1⁻**/**2**/**3**, as evidenced by the negative calculated NICS values of NICS = −65.53/−60.80/−67.08/−60.53 ppm at their geometrical centers, respectively. The spherical aromatic nature of **1**/**1⁻**/**2**/**3** is further evidenced by their iso-chemical shielding surfaces (ICSSs) based on the calculated NICS-ZZ components. As collectively presented in Fig. 4, the areas highlighted in yellow inside the cubes and within about 1.0 Å above the cube surfaces in the vertical direction belong to chemical shielding regions with negative NICS-ZZ values, while the chemical de-shielding regions with positive NICS-ZZ values highlighted in green are located in belt-like areas around the cage waists in the horizontal direction. The ICSSs of metallo-borospherenes **1**/**2**/**3** appear to be similar to that observed in the spherically aromatic *closo* borane dianion O_h $B_6H_6^{2−}$ (Fig. 4(e)), further evidencing that these metallo-borospherenes are spherically aromatic in nature,[57,58] well supporting their high thermodynamic stabilities.
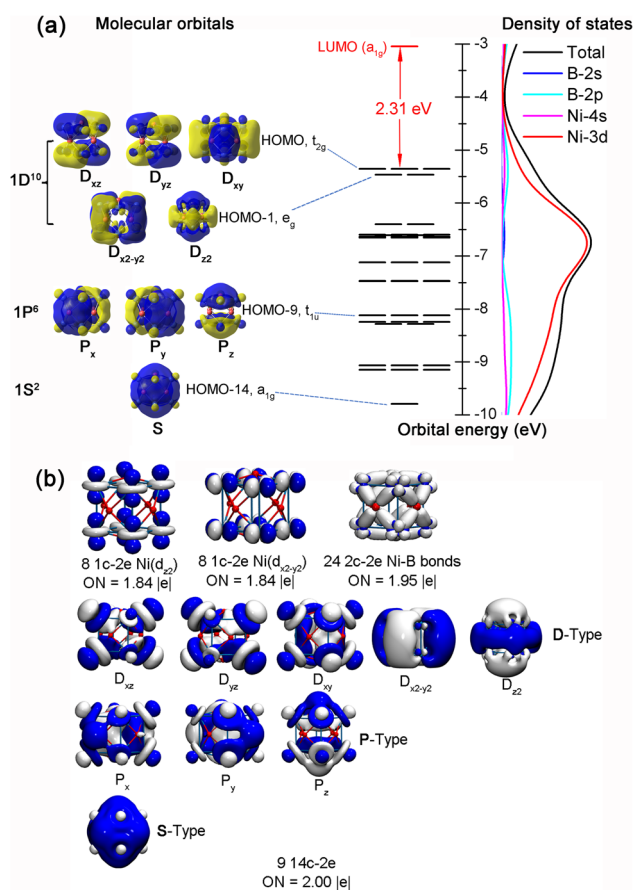

Fig. 3 (a) The $1S^21P^61D^{10}$ 18-electron configuration and calculated densities of states of O_h Ni_8B_6 (**1**). The black and red solid lines refer to occupied and unoccupied orbitals, respectively. (b) AdNDP bonding patterns of O_h Ni_8B_6 (**1**) with the occupation numbers (ONs) indicated.
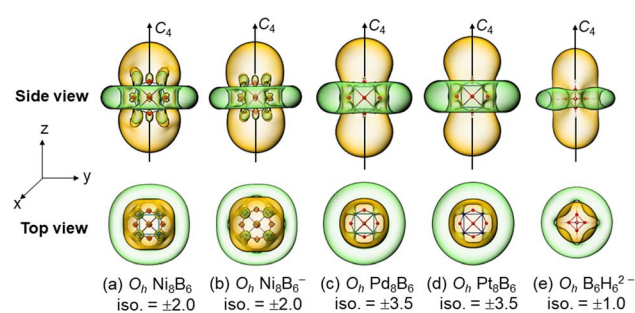

Fig. 4 Calculated iso-chemical shielding surfaces (ICSSs) of (a) O_h Ni_8B_6 (**1**), (b) O_h $Ni_8B_6^−$ (**1⁻**), (c) O_h Pd_8B_6 (**2**), and (d) O_h Pt_8B_6 (**3**), compared with that of (e) O_h $B_6H_6^{2−}$, with the main molecular axes designated as the z axis in the vertical direction. Yellow and green regions stand for chemical shielding and chemical de-shielding areas, respectively.
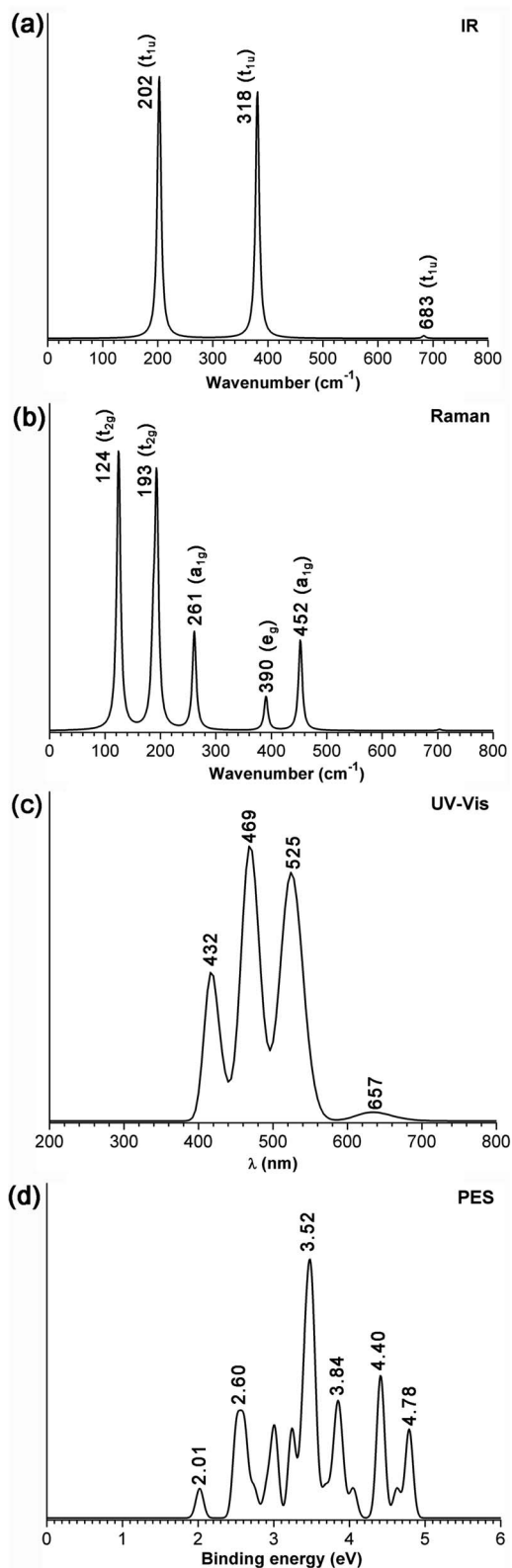
Fig. 5 Simulated (a) IR, (b) Raman, and (c) UV-vis spectra of neutral O_h Ni_8B_6 (**1**), and (d) PE spectroscopy of monoanion $Ni_8B_6^-$ (**1**$^-$) at the PBE0/6-311+G(d) level.

Simulated IR, Raman, UV-vis, and PE spectra

The IR, Raman, and UV-vis spectra of Ni_8B_6 (**1**) are computationally simulated at the PBE0/6-311+G(d) level in Fig. 5(a–c) to assist their future experimental characterization. O_h Ni_8B_6 (**1**) possesses highly simplified IR and Raman spectra due to its high symmetry, including three sharp IR peaks at 202 (t_{1u}), 381 (t_{1u}), and 683 (t_{1u}) cm^{-1} and five Raman active vibrations at 124 (t_{2g}), 193 (t_{2g}), 261 (a_{1g}), 390 (e_g), and 452(a_{1g}) cm^{-1}, respectively. Detailed vibrational analyses indicate that the symmetrical vibrations at 452 cm^{-1} (a_{1g}) represent typical radial breathing modes (RBMs) of the metallosphere which can be used to characterize single-walled hollow boron nanostructures. The simulated UV-vis spectrum of Ni_8B_6 (**1**) exhibits strong absorption peaks at 289, 331, 417, 469, and 525 nm. The strong UV bands around 331, 417, 469, and 525 nm mainly originate from electron transitions from the deep inner shells to the lowest unoccupied molecular orbitals (LUMO, a_{1g}) of Ni_8B_6 (**1**), while UV bands around 289 nm mainly originate from electron transitions from the deep inner shells to the high-lying unoccupied molecular orbitals. As shown in Fig. S7,† O_h Pd_8B_6 (**2**) and O_h Pt_8B_6 (**3**) exhibit similar spectral features to O_h Ni_8B_6 (**1**). The simulated PE spectrum of doublet monoanion $Ni_8B_6^-$ (**1**$^-$) is depicted in Fig. 4(d) at the TD-DFT-PBE0 level. The first vertical detachment energy (VDE) at 2.01 eV for $Ni_8B_6^-$ (**1**$^-$) was calculated as the energy difference between the anionic ground state and the neutral ground state at the optimized anion geometry. $Ni_8B_6^-$ (**1**$^-$) exhibits six well-separated vertical detachment energies centered at VDE = 2.01, 2.60, 3.52, 3.84, 4.40 and 4.78 eV, respectively. It is noticed that $Ni_8B_6^-$ (**1**$^-$) has an extremely low calculated first VDE at 2.01 eV which is even lower than the measured first VDE (2.62 eV) of the prototypical borosphere anion B_{40}^- due to the superb stability of neutral Ni_8B_6 (**1**) which has a superatomic electron configuration as discussed above.

Conclusions

Based on extensive GM searches and first-principles theoretical calculations, we have predicted in this work the GM structures of metallo-borospherenes O_h Ni_8B_6 (**1**), O_h Pd_8B_6 (**2**), O_h Pt_8B_6 (**3**), and O_h $Ni_8B_6^-$ (**1**$^-$). These perfect cubic metallo-borospherenes possess typical spherical aromaticity, with 18 valence electrons occupying nine totally delocalized 14c–2e bonds following the superatomic electron configuration of $1S^2 1P^6 1D^{10}$. The 3D crystal NiB (**4**) as an assembly of O_h Ni_8B_6 (**1**) with an octa-coordinate B atom located exactly at the center of the cubic unit cell exhibits metallic behavior. These high-symmetry metallo-borospherenes and their assembled low-dimensional nanomaterials with interesting geometrical and electronic structures may form novel transition-metal-boron binary nanomaterials as potential chemical catalysts and electronic devices.

Conflicts of interest

There are no conflicts to declare.

Acknowledgements

References

1 B. Albert and H. Hillebrecht, *Angew. Chem., Int. Ed.*, 2009, **48**, 8640.

2 H. W. Kroto, J. R. Heath, S. C. O'Brien, R. F. Curl and R. E. Smalley, *Nature*, 1985, **318**, 162.

3 N. G. Szwacki, A. Sadrzadeh and B. I. Yakobson, *Phys. Rev. Lett.*, 2007, **98**, 166804.

4 A. Sadrzadeh, O. V. Pupysheva, A. K. Singh and B. I. Yakobson, *J. Phys. Chem. A*, 2008, **112**, 13679.

5 H. J. Zhai, Y. F. Zhao, W. L. Li, Q. Chen, H. Bai, H. S. Hu, Z. A. Piazza, W. J. Tian, H. G. Lu, Y. B. Wu, Y. W. Mu, G. F. Wei, Z. P. Liu, J. Li, S. D. Li and L. S. Wang, *Nat. Chem.*, 2014, **6**, 727.

6 Q. Chen, W. L. Li, Y. F. Zhao, S. Y. Zhang, H. S. Hu, H. Bai, H. R. Li, W. J. Tian, H. G. Lu, H. J. Zhai, S. D. Li, J. Li and L. S. Wang, *ACS Nano*, 2015, **9**, 754.

7 Y. J. Wang, Y. F. Zhao, W. L. Li, T. Jian, Q. Chen, X. R. You, T. Ou, X. Y. Zhao, H. J. Zhai, S. D. Li, J. Li and L. S. Wang, *J. Chem. Phys.*, 2016, **144**, 064307.

8 W. J. Chen, Y. Y. Ma, T. T. Chen, M. Z. Ao, D. F. Yuan, Q. Chen, X. X. Tian, Y. W. Mu, S. D. Li and L. S. Wang, *Nanoscale*, 2021, **13**, 3868.

9 Q. Chen, S. Y. Zhang, H. Bai, W. J. Tian, T. Gao, H. R. Li, C. Q. Miao, Y. W. Mu, H. G. Lu, H. J. Zhai and S. D. Li, *Angew. Chem., Int. Ed.*, 2015, **54**, 1.

10 Q. Chen, H. R. Li, C. Q. Miao, Y. J. Wang, H. G. Lu, Y. W. Mu, G. M. Ren, H. J. Zhai and S. D. Li, *Phys. Chem. Chem. Phys.*, 2016, **18**, 11610.

11 Q. Chen, H. R. Li, W. J. Tian, H. G. Lu, H. J. Zhai and S. D. Li, *Phys. Chem. Chem. Phys.*, 2016, **18**, 14186.

12 W. J. Tian, Q. Chen, H. R. Li, M. Yan, Y. W. Mu, H. G. Lu, H. J. Zhai and S. D. Li, *Phys. Chem. Chem. Phys.*, 2016, **18**, 9922.

13 J. Barroso, S. Pan and G. Merino, *Chem. Soc. Rev.*, 2022, **51**, 1098.

14 W. Liang, J. Barroso, S. Jalife, M. Orozco-Ic, X. Zarate, X. Dong, Z. Cui and G. Merino, *Chem. Commun.*, 2019, **55**, 7490.

15 H. Bai, Q. Chen, H. J. Zhai and S. D. Li, *Angew. Chem., Int. Ed.*, 2014, **53**, 1.

16 T. T. Chen, W. L. Li, W. J. Chen, X. H. Yu, X. R. Dong, J. Li and L. S. Wang, *Nat. Commun.*, 2020, **11**, 2766.

17 X. Y. Zhao, M. Yan, Z. H. Wei and S. D. Li, *RSC Adv.*, 2020, **10**, 34225.

18 Y. Zhang, X. Y. Zhao, M. Yan and S. D. Li, *RSC Adv.*, 2020, **10**, 29320.

19 X. Dong, Yu. Liu, X. Liu, S. Pan, Z. Cui and G. Merino, *Angew. Chem., Int. Ed.*, 2022, **61**, e202208152.

20 Y. Zhang, X. Q. Lu, M. Yan and S. D. Li, *ACS Omega*, 2021, **6**, 10991.

21 T. Yu, Y. Gao, D. Xu and Z. Wang, *Nano Res.*, 2018, **11**, 354.

22 Q. Q. Yan, T. Zhang, Y. Y. Ma, Q. Chen, Y. W. Mu and S. D. Li, *Nanoscale*, 2022, **14**, 11443.

23 M. Z. Ao, F. Zhang, Y. Y. Ma, Y. W. Mu and S. D. Li, *Nanoscale*, 2023, **15**, 2377.

24 P. Cui, H. S. Hu, B. Zhao, J. T. Miller, P. Cheng and J. Li, *Nat. Commun.*, 2015, **6**, 6331.

25 N. Masciocchi, S. Galli, V. Colombo, A. Maspero, G. Palmisano, B. Seyyedi, C. Lamberti and S. Bordiga, *J. Am. Chem. Soc.*, 2010, **132**, 7902.

26 H. C. Hu, H. S. Hu, B. Zhao, P. Cui, P. Cheng and J. Li, *Angew. Chem., Int. Ed.*, 2015, **54**, 11681.

27 C. A. Barboza, A. Gambetta, R. Arratia-Pérez, P. L. Rodríguez-Kessler, A. Muñoz-Castro and D. MacLeod-Carey, *Polyhedron*, 2021, **195**, 114878.

28 T. B. Tai and M. T. Nguyen, *Chem. Comm.*, 2013, **49**, 913.

29 J. C. Guo, L. Y. Feng, C. Dong and H. J. Zhai, *New J. Chem.*, 2020, **44**, 7286.

30 Y. Zhao, X. Chen and J. Li, *Nano Res.*, 2017, **10**, 3407.

31 C. Adamo and V. Barone, *J. Chem. Phys.*, 1999, **110**, 6158.

32 V. N. Staroverov, G. E. Scuseria, J. M. Tao and J. P. Perdew, *J. Chem. Phys.*, 2003, **119**, 12129.

33 R. Krishnan, J. S. Binkley, R. Seeger and J. A. Pople, *J. Chem. Phys.*, 1980, **72**, 650.

34 D. Andrae, U. Haeussermann, M. Dolg, H. Stoll and H. Preuss, *Theor. Chim. Acta*, 1990, **77**, 123.

35 R. Bauernschmitt and R. Ahlrichs, *Chem. Phys. Lett.*, 1996, **256**, 454.

36 M. J. Frisch, *et al.*, *Gaussian 09, Revision D.01*, Gaussian Inc., Wallingford, CT, 2009.

37 P. E. D. Glendening, J. K. Badenhoop, A. E. Reed, J. E. Carpenter, J. A. Bohmann, C. M. Morales, C. R. Landis and F. Weinhold, *NBO 6.0*, 2013.

38 J. V. Vondele, M. Krack, F. Mohamed, M. Parrinello, T. Chassaing and J. Hutter, *Comput. Phys. Commun.*, 2005, **167**, 103.

39 D. Y. Zubarev and A. I. Boldyrev, *Phys. Chem. Chem. Phys.*, 2008, **10**, 5207.

40 P. v. R. Schleyer, C. Maerker, A. Dransfeld, H. Jiao and N. J. v. E. Hommes, *J. Am. Chem. Soc.*, 1996, **118**, 6317.

41 Z. Chen, C. S. Wannere, C. Corminboeuf, R. Puchta and P. V. R. Schleyer, *Chem. Rev.*, 2005, **105**, 3842.

42 T. Lu and F. Chen, *J. Comput. Chem.*, 2012, **33**, 580.

43 W. Humphrey, A. Dalke and K. Schulten, *J. Mol. Graphics*, 1996, **14**, 33.

44 G. Kresse and J. Furthmüller, *Comput. Mater. Sci.*, 1996, **6**, 15.

45 G. Kresse and J. Furthmüller, *Phys. Rev. B: Condens. Matter Mater. Phys.*, 1996, **54**, 11169.

46 P. E. Blöchl, *Phys. Rev. B: Condens. Matter Mater. Phys.*, 1994, **50**, 17953.

47 G. Kresse and D. Joubert, *Phys. Rev. B: Condens. Matter Mater. Phys.*, 1999, **59**, 1758.

48 J. P. Perdew, K. Burke and M. Ernzerhof, *Phys. Rev. Lett.*, 1996, **77**, 3865.

49 J. P. Perdew, K. Burke and M. Ernzerhof, *Phys. Rev. Lett.*, 1997, **78**, 1396.

50 I. V. Solovyev and P. H. Dederichs, *Phys. Rev. B: Condens. Matter Mater. Phys.*, 1994, **50**, 16861.

51 V. I. Anisimov, J. Zaanen and O. K. Andersen, *Phys. Rev. B: Condens. Matter Mater. Phys.*, 1991, **44**, 943.

52 Y. Gao, X. Wang, J. Ma, Z. Wang and L. Chen, *Chem. Mater.*, 2015, **27**, 3456.

53 F. Zhou, M. Cococcioni, C. Marianetti, D. Morgan and G. Ceder, *Phys. Rev. B: Condens. Matter Mater. Phys.*, 2004, **70**, 235121.

54 A. Togo, F. Oba and I. Tanaka, *Phys. Rev. B: Condens. Matter Mater. Phys.*, 2008, **78**, 134106.

55 P. Pyykkö, *J. Phys. Chem. A*, 2015, **119**, 2326.

56 E. Lugscheider, O. Knotek and H. Reimann, *Monatsh. Chem.*, 1974, **105**, 80.

57 G. Merino, T. Heine and G. Seifert, *Chem. Eur. J.*, 2004, **10**, 4367.

58 G. Merino, M. Solà, I. Fernández, C. Foroutan-Nejad, P. Lazzeretti, G. Frenking, H. L. Anderson, D. Sundholm, F. P. Cossío, M. A. Petrukhina, J. Wu, J. I. Wu and A. Restrepo, *Chem. Sci.*, 2023, **14**, 5569.